HHS Public Access

Author manuscript

Cell Rep. Author manuscript; available in PMC 2025 May 15.

Published in final edited form as:

Cell Rep. 2025 January 28; 44(1): 115090. doi:10.1016/j.celrep.2024.115090.

Cell-type-specific auditory responses in the striatum are shaped by feedforward inhibition

Mélanie Druart[1], **Megha Kori**[1], **Corryn Chaimowitz**[1], **Catherine Fan**[1], **Tanya Sippy**[1,2,*]

[1]Department of Psychiatry and Neuroscience & Physiology, New York University Grossman School of Medicine, New York, NY 10016, USA

[2]Lead contact

SUMMARY

The posterior "tail" region of the striatum receives dense innervation from sensory brain regions and is important for behaviors that require sensorimotor integration. The output neurons of the striatum, D1 and D2 striatal projection neurons (SPNs), which make up the direct and indirect pathways, are thought to play distinct functional roles, although it remains unclear if these neurons show cell-type-specific differences in their response to sensory stimuli. Here, we examine the strength of synaptic inputs onto D1 and D2 SPNs following the stimulation of upstream auditory pathways. We report that auditory-evoked depolarizations onto D1 SPN responses are stronger and faster. This is due to differences in feedforward inhibition, with fast-spiking interneurons forming stronger synapses onto D2 SPNs. Our results support a model in which differences in feedforward inhibition enable the preferential recruitment of D1 SPNs by auditory stimuli, positioning the direct pathway to initiate sound-driven actions.

Graphical abstract

*Correspondence: tanya.sippy@nyulangone.org.

AUTHOR CONTRIBUTIONS

T.S. and M.D. contributed to the study design and wrote the paper. M.D. and M.K. performed *in vivo* electrophysiology experiments. M.D. conducted *ex vivo* electrophysiology experiments, analyzed the data, and performed the *in vivo* fiber photometry experiments. C.C. performed virus injections, histology, immunohistochemistry, and imaging of rabies-injected mice, and M.D. and C.F. performed analysis using the BrainJ pipeline. M.K. created a database for all *in vivo* data and wrote the custom code to analyze these data.

DECLARATION OF INTERESTS

The authors have no interests to declare.

SUPPLEMENTAL INFORMATION

Supplemental information can be found online at https://doi.org/10.1016/j.celrep.2024.115090.

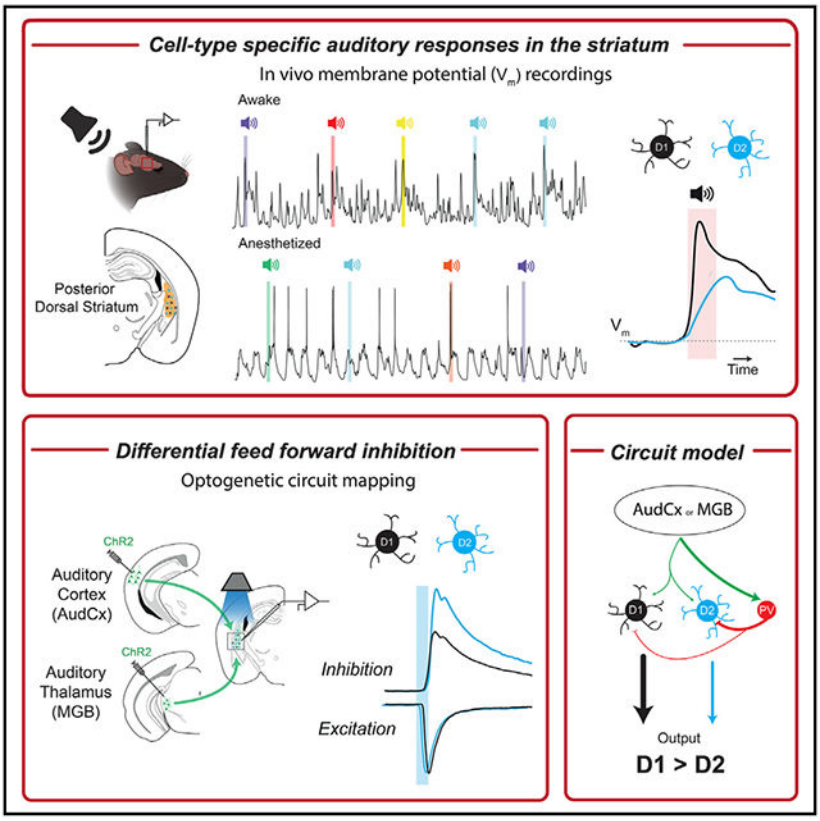

In brief

How neurons in the posterior striatum encode auditory information is not well understood. Druart et al. report that direct pathway neurons in the striatum respond more strongly to auditory stimuli. This is underscored by differences in feedforward inhibition by PV+ interneurons onto these neurons from the primary auditory cortex and auditory thalamus.

INTRODUCTION

The ability to use sensory information to guide our actions is a fundamental ability of brain circuitry that is crucial for survival. The input nucleus of the basal ganglia, the striatum, is thought to integrate contextual, motor, and reward information to control action initiation and selection. Several anatomical investigations have confirmed the presence and organization of functional sensory inputs throughout the rodent dorsal striatum.[1–3] It is well established that primary sensory cortical areas and sensory thalamic nuclei project to this region, making glutamatergic connections onto striatal neurons in a cell-type-specific manner.[4] However, how this connectivity is related to the responsiveness of these neurons to sensory stimuli remains unclear.

Striatal neurons are predominantly GABAergic striatal projection neurons (SPNs) that can be divided into two main classes depending on their projection patterns and expression of dopamine receptors: D1-expressing SPNs (D1 SPNs) make up the “direct” pathway and directly project to the output nuclei of the basal ganglia, while D2-expressing SPNs

(D2 SPNs) make up the “indirect” pathway and project to the globus pallidus. D1 SPN activity has been classically associated with increased movement, while D2 SPN activity is associated with reduced movement.[5] Yet, pathway-specific differences in the activity of these neural populations have been hard to reveal during spontaneous movements and/or locomotion.[6–9] In contrast, we previously reported that during sensory-evoked movements, D1 SPNs are preferentially activated before D2 SPNs and that this might serve to initiate sensory-triggered actions.[10] Here, we investigate the synaptic responses of striatal neurons resulting from sensory inputs both *in vivo* and *ex vivo*. We focused on the posterior striatum (pStr) that gets rich sensory input, particularly from auditory areas such as the primary auditory cortex (A1) and auditory thalamus (medial geniculate nucleus [MGB]).

We measured the membrane potential (V_m) response of D1 and D2 SPNs to auditory stimuli in awake and anesthetized mice and report that auditory-evoked responses are more robust in D1 SPNs compared with D2 SPNs. *Ex vivo* experiments revealed that feedforward inhibition is stronger on D2 SPNs. Local parvalbumin (PV) interneurons make stronger connections to D2 SPNs compared to D1 SPNs and modulate the response of these neurons to auditory stimuli *in vivo*. Our results show that direct pathway neurons of the pStr respond more robustly to auditory stimuli, a difference that is supported by cell-type-specific differences in the connectivity of the local inhibitory network.

RESULTS

In vivo auditory-evoked synaptic responses in D1 and D2 SPNs

We played auditory stimuli (7 chords, with center frequencies ranging from 5.1 to 31.9 Hz, logarithmically spaced) to head-fixed, awake mice and simultaneously obtained V_m recordings in the pStr (Figure 1A).[11] Post hoc biocytin labeling allowed us to determine the precise location of recorded neurons in the pStr (Figures 1B, S1E, and S2A; Table S1). We employed mice that expressed channelrhodopsin-2 (ChR2) in D2 neurons (D2-Cre[12] x Ai32[13]) and used the “optopatch” method to distinguish ChR2+ D2 SPNs from ChR2−, putative D1 SPNs.[14–16] In brief, after a stable recording was established, 500-ms-long pulses of blue light were applied via the patch pipette, resulting in short-latency depolarizations and action potential (AP) firing in neurons expressing ChR2 (Figure 1C). SPNs were readily identifiable from other cell types in the striatum given their (1) low spontaneous firing rates (typically less than 0.1 Hz) and hyperpolarized V_m (−93.09 to −58.41 mV), (2) low input resistances (66.2–191.4 MΩ), and (3) high rheobase values (75–700 pA; Figures S1A–S1D).[17] D2 SPNs were light responsive, and ChR2− neurons showed mostly no response to light or had a slight hyperpolarization due to recurrent connectivity from nearby ChR2+ D2 SPNs, which are GABAergic.

We recorded 21 D2 SPNs and 27 D1 SPNs in awake mice that all displayed spontaneous subthreshold V_m dynamics (Figure 1D). Of these, 12/21 (57%) D2 SPNs and 12/27 (44%) D1 SPNs were characterized as having a response to at least 1 chord, with no difference in these proportions (chi-square test, $p = 0.56$) (Figure 1F). In this subset, we found that the grand average V_m auditory-evoked response of D1 SPNs was larger than that of D2 SPNs ($p = 0.02$, two-way RM Anova) (Figures 1G and 1H). Indeed, the delta V_m deflection to the chord of maximum response in D1 SPNs was significantly larger (D1 = 10.58 ± 1.76 mV,

D2 = 5.84 ± 0.95 mV; $p = 0.03$; mean ± SEM, Student's *t* test) (Figure 1I) and faster than D2 SPNs (D1 = 0.489 ± 0.099 mV/ms, D2 = 0.200 ± 0.124 mV/ms; $p = 0.01$; mean ± SEM, Student's *t* test) (Figure 1J), culminating in a greater overall depolarization, or area under the curve (AUC) (D1 = 13.7 ± 2.02, D2 = 8.36 ± 1.39; $p = 0.04$; mean ± SEM, Student's *t* test) (Figure 1K). D1 SPNs responded to a similar number of chords to D2 SPNs (Figures S1F and S1G) and displayed similar response reliability (Figures S1G and S1H) but had higher response fidelity (Figure S1I).

Given that sensory-evoked movements influence the responsiveness of striatal neurons to sensory stimuli,[16] we repeated these experiments in mice anesthetized with ketamine/xylazine. These recordings revealed UP and DOWN states of the V_m that are typical of anesthesia[14,15,18–20] (Figures 2A and 2B; Table S2). Similar to our findings in awake mice, the proportion of auditory-responsive cells did not differ between D1 and D2 SPNs, with 18/23 D1 SPNs and 19/23 D2 SPNs showing responses (chi-square test, $p = 0.90$) (Figure 2C). In addition, the grand average V_m auditory-evoked response of D1 SPNs was larger than that of D2 SPNs ($p = 0.02$, two-way RM Anova) (Figures 2D and 2E) and demonstrated a larger delta V_m (D1 = 14.73 ± 1.48 mV, D2 = 8.45 ± 1.00 mV; $p = 0.001$; mean ± SEM, Student's *t* test) (Figure 2F), a faster rate of rise (D1 = 0.622 ± 0.090 mV/ms, D2 = 0.297 ± 0.043 mV/ms; $p = 8 \times 10^{-4}$; mean ± SEM, Mann Whitney) (Figure 2G), and a larger overall response, as measured by the AUC (D1 = 15.58 ± 1.89, D2 = 9.27 ± 1.15; $p = 0.007$; mean ± SEM, Student's *t* test) (Figure 2H). Under anesthesia, D1 SPNs tended to respond to more chords than D2 SPNs (Figure S2B) but showed similar response stability and reliability (Figures S2C–S2E). Because each neuron had distinct preferred frequencies, potentially complicating comparisons between groups, we performed a set of experiments in which we played white noise bursts of varying intensities (Figure 2I). D1 SPNs showed larger responses at all intensities tested ($p = 0.006$, two-way RM Anova) (Figure 2J). Finally, to understand if the state of the V_m might differentially affect the responses of these neuron types, we analyzed the amplitudes of evoked responses for stimuli arriving in the DOWN state versus the UP state, finding that responses were larger in the DOWN state ($p = 3 \times 10^{-4}$, two-way RM Anova)(Figures 2K and 2L).

Cell-type-specific connectivity from auditory thalamus and AudCx onto D1 and D2 SPNs

The cell-type-specific responses observed *in vivo* may be attributable to differences in intrinsic excitability between direct and indirect pathway neurons. However, D2 SPNs are more excitable than D1 SPNs *in vivo* (Figures S1A–S1D), a difference that would render them more, rather than less, responsive to inputs.[21] It could also arise from differences in connectivity from upstream auditory brain regions such as the MGB of the thalamus and the A1 of the cortex. To test this, we made use of rabies viruses to transsynaptically trace afferent inputs to both SPN cell types.[22] We injected helper viruses (AAV-FLEX-TVA and AAV-FLEX-N2cG) into the pStr of either D1-Cre or A2A-Cre mice and later injected pseudotyped, G-deficient CVS-N2c rabies expressing GFP[23] (EnVA-N2cΔG-GFP) into the same region (Figures 3A and S3A). This resulted in intense GFP expression in the MGB and auditory cortex (AudCx; including the primary and secondary AudCxs) (Figures 3B and S3B). We then calculated the percentage of neurons from the AudCx and MGB projecting

to D1 or D2 SPNs, finding no difference from either region ($p = 0.95$, two-way RM Anova) (Figures 3C and S3B–S3D; Table S3).

We next set out to test the relative strength of A1 and MGB connections to pStr D1 and D2 SPNs. First, in D1-tdTomato or D2-Cre x Ai14 mice, we expressed ChR2 in the A1 (Figures 3D and S4A). Weeks later, we obtained voltage-clamp whole-cell recordings in brain slices from D1 or D2 SPNs (identified by the presence or absence of tdTomato). Recordings were made from 14 pairs of neighboring (within 80 μm) D1 and D2 SPNs patched sequentially. Brief (8 ms) flashes of blue light resulted in excitatory postsynaptic currents (EPSCs) when measured at a holding potential of −80 mV and inhibitory postsynaptic currents (IPSCs) at +10 mV in both D1 and D2 SPNs (Figure 3E). Comparing ChR2-evoked EPSCs in D1 and D2 SPNs revealed no significant difference in amplitude (D1 = 209.4 ± 56 pA, D2 = 152.8 ± 27 pA, $p = 0.67$; mean ± SEM, Wilcoxin matched-pairs test) (Figure 3F). IPSC amplitudes were also not statistically different between D1 and D2 SPNs (D1 = 134.8 ± 30 pA, D2 = 235.7 ± 62 pA, $p = 0.12$; mean ± SEM, Student's paired *t* test) (Figure 3G). However, the ratio of the EPSC to IPSC amplitudes (E/I ratio) was statistically larger for D1 SPNs than D2 SPNs (D1 = 2.27 ± 0.44, D2 = 1.41 ± 0.45, $p = 0.01$; mean ± SEM, Wilcoxin matched-pairs test) (Figure 3H).

In separate animals, we infected MGB neurons with ChR2, and the resulting EPSC and IPSC responses were measured in 14 pairs of D1 and D2 SPNs (Figures 3I and 3). As with the A1, we observed no difference in EPSC amplitudes (D1 = 137.3 ± 19.9 pA, D2 = 161.0 ± 34.0 pA, $p = 0.44$; mean ± SEM, Student's paired *t* test) (Figure 3K). However, MGB-evoked IPSCs were larger in D2 SPNs than in D1 SPNs (D1 = 104.6 ± 28.8 pA, D2 = 279.1 ± 78.5 pA, $p = 0.003$; mean ± SEM, Wilcoxin matched-pairs test) (Figure 3L), resulting in a significantly greater E/I ratio in D1 SPNs (D1 = 2.92 ± 0.78, D2 = 0.97 ± 0.26, $p = 0.007$; mean ± SEM, Wilcoxin matched-pairs test) (Figure 3M). We observed no difference in the probability of connection from either the A1 or MGB onto D1 or D2 SPNs (Figures S4B and S4G), and IPSCs were confirmed to be of polysynaptic origin (Figures S4C–S4H). Overall, these results reveal that D1 and D2 SPNs differ in the strength of feedforward inhibition, with D2 SPNs receiving more inhibition than D1 SPNs.

Feedforward inhibition by PV interneurons contributes to cell-type-specific auditory responses in the striatum

It is possible that this difference in E/I ratio contributed to the larger depolarizations of D1 SPNs to auditory stimuli we report *in vivo*. To test this, we sequentially patched D1 and D2 SPNs in current-clamp mode to assess the overall impact of auditory afferent optogenetic stimulation on the V_m of D1 and D2 SPNs. In line with our *in vivo* findings, D1 SPNs were found to be less excitable than D2 SPNs (Figures S4K–S4O). Despite this, A1 ChR2-evoked depolarizations were larger in D1 SPNs than D2 SPNs (D1 = 11.51 ± 2.4 mV, D2 = 6.42 ± 1.34 mV; $p = 0.01$; mean ± SEM, Student's paired *t* test) (Figures 3N and S4D). We next blocked feedforward inhibition with gabazine, a $GABA_A$ antagonist. This resulted in comparable A1-evoked responses between D1 and D2 SPNs (D1 = 8.78 ± 1.91 mV, D2 = 7.96 ± 1.55 mV; $p = 0.61$; mean ± SEM, Student's paired *t* test) (Figures 3O and S4E). When stimulating MGB terminals, the size of the evoked response was also larger in D1

SPNs (D1 = 10.47 ± 1.53 mV, D2 = 7.165 ± 1.11 mV; $p = 0.007$; mean ± SEM, Student's paired *t* test) (Figures 3P and S4I), a difference that was again blocked by gabazine (D1 = 13.87 ± 2.56 mV, D2 = 14.47 ± 2.51 mV; $p = 0.82$; mean ± SEM, Student's paired *t* test) (Figures 3Q and S4J).

Fast-spiking interneurons (FSIs) are well known for exerting powerful and fast feedforward inhibition in the striatum.[24,25] We therefore wondered whether they differentially innervate D1 and D2 SPNs. We analyzed recordings from tdTomato− neurons in which the neuron was an FSI, recognizable by its distinct firing properties and narrow spike width. Notably, these neurons exhibited a high rate of connectivity to both the A1 and MGB and were easily driven to fire APs upon auditory afferent stimulation, consistent with other studies[4,26] (Figures S5A–S5C). We then set out to test the strength of the connections FSIs make to D1 and D2 SPNs. Because FSIs in the striatum are known to express PV, we expressed ChR2 in PV-Cre mice[27] and made *ex vivo* slices in which we sequentially patched D1 and D2 SPNs in a voltage clamp at +10 mV while briefly (8 ms) stimulating PV interneurons with blue light (Figures 4A, S5D, and S5E). The PV interneuron-evoked IPSCs onto D2 SPNs were significantly larger (D1 = 90.3 ± 11.3 pA, D2 = 148.1 ± 22.4 pA, $p = 0.02$; mean ± SEM, Student's paired *t* test) (Figures 4B and 4C; Table S4). In addition, the paired-pulse ratio (PPR) was lower in D2 SPNs, indicating a higher initial probability of release at these synapses (Figures S5G).

To better understand the contribution FSIs make to the cell-type-specific effects in auditory-evoked responses, we inhibited these neurons by infecting PV interneurons in the pStr with the inhibitory designer receptor exclusively activated by designer drugs, hM4Di ($DREADD_i$). We subsequently made *ex vivo* slices and performed optogenetic circuit mapping of the A1 and MGB onto pairs of D1 and D2 SPNs. Upon activation of the $DREADD_i$ with clozapine N-oxide (CNO), we found that the light-evoked EPSP resulting from either A1 or MGB inputs was similar to D1 and D2 SPNs (A1: D1 = 10.81 ± 1.79 mV, D2 = 11.10 ± 1.86 mV; $p = 0.85$; mean ± SEM, Student's paired *t* test; MGB: D1 = 7.51 ± 1.19 mV, D2 = 8.13 ± 1.28 mV; $p = 0.67$; mean ± SEM, Student's paired *t* test) (Figures 4D and 4E). After confirming that PV interneurons respond to auditory stimuli in awake mice (Figure S6), we crossed PV-Cre mice with A2A-Flp mice and injected AAV-DIO-hM4Di and AAV-FlpO-GCaMP6f into the pStr so that we could use fiber photometry to measure the response of D2 SPNs to white-noise bursts of varying intensities with and without inhibition of PV interneurons (Figure 4F). We found that D2 SPNs showed larger and faster evoked fluorescence responses when mice were injected with CNO versus saline ($p = 0.004$, two-way RM ANOVA) (Figures 4G, 4H, and S6D). Taken together, these results suggest that PV interneurons make cell-type-specific connections onto D1 and D2 SPNs and contribute to their differential responsivity to auditory stimuli.

DISCUSSION

In this study, we measured the subthreshold voltage activations evoked by auditory stimuli in the pStr in awake and anesthetized mice. These recordings revealed a bias of these responses onto D1 SPN neurons of the direct pathway. Optogenetic circuit mapping *ex vivo* revealed differences in feedforward inhibition onto D1 and D2 SPNs, with D1 SPNs showing a higher

E/I ratio and receiving weaker inhibition from FSIs than D2 SPNs, and inhibition of PV interneurons *ex vivo* and *in vivo* demonstrated that these cells contribute to this difference. Our results put forward a circuit mechanism by which these cell types can be differentially recruited by auditory stimuli to mediate behavior.

Cell-type-specific sensory responses in the striatum across modalities and behaviors

Given that the striatum receives input from many sensory cortical and subcortical areas, it is interesting to consider how our results compare to those of other modalities. Recordings made from neurons in the dorsolateral striatum (DLS) revealed that whisker-evoked synaptic responses were significantly larger in direct pathway neurons.[20,28] The A1 also shows substantial innervation of the dorsomedial striatum,[2] and it is unclear if these inputs exhibit patterns of innervation onto the direct and indirect pathway neurons like those we demonstrate here for the pStr.

Several studies have examined how output pathways of the striatum are activated in response to sensory stimuli that trigger behavior. Previous work from our group demonstrated stronger somatosensory-triggered subthreshold responses in D1 SPNs both before and after mice learned to perform a whisker detection task.[10,17] Imaging studies that have shown larger cue-evoked activity in the direct pathway in the DLS during an auditory-cue-triggered motor task.[29] Therefore, it is possible that D1 SPNs are specialized to mediate sensory-driven actions, especially after sensorimotor learning.[17,30,31] While the role that sensory-evoked responses in D2 neurons play in behavior is yet to be fully elucidated, some studies point to freezing and avoidance responses under certain conditions.[31]

Feedforward inhibition as a mediator of cell-type-specific sensory responses in the striatum

Our finding that the E/I ratio is higher onto D1 SPNs in both A1 and MGB inputs is consistent with what was previously found for insula inputs to this region and may, therefore, be a general property of inputs to the pStr.[31] While fast-spiking, PV+ interneurons make up a small percentage of neurons in the striatum, they are known to be readily recruited by cortical inputs[4] and active during periods when SPNs are under the influence of strong cortical and subcortical as well as dopaminergic inputs, as is the case for movement and learning.[32–34] Because they make abundant connections to nearby SPNs, PV interneurons can then powerfully regulate the responsiveness of these neurons to incoming inputs.[24,35–40] In the case of the pStr, a region thought to be important for mediating avoidance, it is possible that increased activation of D1 SPNs, mediated by the differential connectivity of PV interneurons onto SPN subtypes, allows for navigation away from novel, and potentially threatening, stimuli.[31]

An important outstanding question is the role that dopamine and acetylcholine might play in shaping the responsiveness of D1 and D2 SPNs to auditory stimuli, both before and after learning. Dopamine projections to this region are particularly active during the presentation of novel auditory stimuli and in response to aversive outcomes.[30,41–43] Acetylcholine release, via nicotinic receptors on presynaptic dopamine terminals,[44,45] causes the release of dopamine, although it is still unknown if acetylcholine is released in the pStr in response

to auditory cues. Future work may examine how these processes work in parallel[46] to determine how the output pathways of the pStr are differentially recruited during both innate and learned behaviors.

Limitations of the study

It is unclear how our results in the pStr might compare with other striatal subregions. For example, in the dorsal striatum, it was previously found that FSIs are more likely to connect with D1 SPNs.[47] This is not entirely surprising given that it is increasingly clear that the striatum is made up of different subregions, each of which may have distinct connectivity patterns that relate to its function.[40,48] While not the focus of this study, a side-by-side comparison of FSI-to-SPN connectivity in the DMS, DLS, NAc (nucleus accumbens), and pStr would be informative. We show here that inhibition of PV interneurons increases the auditory-evoked responses of D2 SPNs *in vivo*. While we expect a similar result in D1 SPNs, a direct comparison would require the simultaneous monitoring of D1 and D2 SPNs in the same animals while manipulating PV interneurons. Performing such experiments during behavior would further help to relate these findings to function.

RESOURCE AVAILABILITY

Lead contact

Further information and requests for resources and reagents should be directed to and will be fulfilled by the lead contact, Tanya Sippy (tanya.sippy@nyulangone.org).

Materials availability

No new materials were generated in this study.

Data and code availability

- All *in vivo* and *ex vivo* electrophysiology data have been deposited at Zenodo and are publicly available as of the date of this publication. All other data are available from the lead contact upon request.
- All original code has been deposited at Zenodo and is publicly available at the time of this publication. DOIs are listed in the key resources table.
- Any other information required to reanalyze the data reported in this paper is available from the lead contact upon request

STAR★METHODS

EXPERIMENTAL MODEL AND STUDY PARTICIPANT DETAILS

All experiments were carried out with 8–16-week-old male and female mice >15 g in accordance with National Institutes of Health (NIH) guidelines and protocols approved by the NYU Langone Health (NYULH) Institutional Animal Care and Use Committee (protocol# PROTO201900059). No effects of sex are reported. Mice were bred in-house on a C57Bl/6J background and housed in a reverse light/dark cycle (light 11 p.m. to 11 a.m.), at a temperature of 22 ± 2°C with food

available *ad libitum*. Mice were group housed with littermates of the same sex during experimental procedures. The following strains used in this proposal were sourced from Jackson Laboratories: Ai9: B6.Cg-*Gt(ROSA)26Sor*$^{tm9(CAG\text{-}tdTomato)Hze}$/J (JAX:007909), Ai14: B6.Cg-*Gt(ROSA)26Sor*$^{tm14(CAG\text{-}tdTomato)Hze}$/J (JAX:007914), Ai32: B6.Cg-*Gt(ROSA)26Sor*$^{tm32(CAG\text{-}COP4*H134R/EYFP)Hze}$/J (JAX: 012569), Drd1a-tdTomato: B6.Cg-Tg(Drd1a-tdTomato)6Calak/J (JAX: 016204), PV-Cre: B6.129P2-*Pvalb*$^{tm1(cre)Arbr}$/J (JAX:017320). The following bacterial artificial chromosome (BAC) transgenic mouse strains used in this proposal were sourced from the Mutant Mouse Regional Resource Centers (MMRRC): A2A-Cre: B6.FVB(Cg)-Tg(Adora2a-cre)KG139Gsat/Mmucd (MMRRC_036158-UCD), D2-Cre: B6.FVB(Cg)-Tg(Drd2-cre)ER44Gsat/Mmucd (MMRRC_032108-UCD), EY262-Cre: B6.FVB(Cg)-Tg(Drd1-cre)EY262Gsat/Mmucd (MMRRC_030989-UCD). A2A-Flp knock-in mice were provided by the laboratory of R. Costa at Columbia University.

METHOD DETAILS

Animals: All experiments were carried out with 6–16-week-old male and female mice in accordance with protocols approved by the NYU Langone Health (NYULH) Institutional Animal Care and Use Committee (protocol #PROTO201900059). D1-Cre, A2A-Cre and D2-Cre bacterial artificial chromosome (BAC) transgenic mice were obtained from Gene Expression Nervous System Atlas (GENSAT; founder line EY262 for D1-Cre, KG139 for A2A-Cre and ER44 for D2-Cre), and purchased through the Mutant Mouse Regional Resource Centers (MMRRC). PV-Cre mice were purchased from Jackson Labs. For *in vivo* optopatching experiments, D2-Cre mice were crossed with lox-stop-lox (LSL) Channelrhodopsin reporter mice (Ai32, JAX: 012569) to obtain D2-Cre x Ai32 mice. For *ex vivo* slice experiments, Drd1a-tdTomato (JAX: 016204) **or** D2-Cre and PV-Cre mice crossed with Lox-Stop-Lox-tdTomato mice (Ai9, JAX: 007909 and Ai14, JAX:007914) were used.

The mice were housed in a reverse light/dark cycle (light 11 p.m. to 11 a.m.), at a temperature of 22 ± 2°C with food available *ad libitum*.

In vivo electrophysiology: D2-Cre x Ai32 mice were implanted with a light-weight metal head post under isoflurane anesthesia. Seven to ten days later, mice underwent habituation to head fixation for 3 days in increasing time increments. On the day of the recordings, a small (less than 1 mm diameter) craniotomy made under isoflurane anesthesia over the pStr (stereotaxic coordinates: 1.7 mm posterior and 3.0 mm lateral to bregma). For awake recordings, mice were allowed to recover from anesthesia for two to 4 h, then transferred directly to the setup. For anesthetized recordings, mice were first injected with a mix of Ketamine/Xylazine (100 mg/kg; 10 mg/kg). Afterward, whole-cell patch clamp recordings were made as previously described.[45] 6–8 MΩ glass pipettes were filled with a solution containing (in mM): 135 K-methyl sulfonate, 5 KCl, 0.1 EGTA-KOH, 10 HEPES, 2 NaCl, 5 MgATP, 0.4 Na2GTP, 10 Na2-phosphocreatine, to which 2–4 mg/mL of biocytin was added. All patch clamp recordings *in vivo* were obtained in current-clamp mode without injection of any current, except during the characterization of intrinsic electrophysiological properties, and the V_m was not corrected for liquid junction potentials. V_m signals were amplified using a Multiclamp 700B amplifier but digitized at 20 kHz using

National Instruments acquisition boards (BNC 2110) and recorded in a MATLAB software (Wavesurfer, HHMI Janelia Research Campus).

At the start of each recording, a series of increasing current steps from −200 with increments of +25 pA was injected into each neuron. The optopatcher was used for the online identification (A-M systems, WA USA). Light steps of 500 ms were delivered via a 470 nm LED (Thor labs) through an optic fiber (power at the tip of the fiber was 1.5–3 mW) inserted into the patch-pipette while recording the responses in whole-cell configuration. Positive cells responded to light pulses with step-like depolarization, often exhibiting AP, while negative cells displayed no response or a small hyperpolarization. We proceeded with the recording if the neuron displayed both a stable resting V_m and overshooting action potentials. The series resistance of the recordings was between 25 and 50 MΩ. Our measurements of V_m in SPNs during sound presentation included between 4 and 25 trials for each chord with 3–5 s inter-trial intervals. Sound presentations consisted of 100 ms chords containing (12 pure tones spaced .1–.75 octaves apart) with the following center frequencies: (6.2, 7.9). In other experiments, sound presentations consisted of 100 ms bursts of white noise at varying intensities (40 db, 60 dB, 75 dB and 90 dB). Each stimulus was given in a randomized manner with equivalent probability.

Optogenetic circuit mapping in *ex vivo* slices: Drd1a-tdTomato x PV-Cre mice were injected under isoflurane anesthesia with an adeno-associated virus (AAV) serotype 5-expressing double-floxed inverted reading frame humanized ChR2(H134R) fused to YFP under the control of the CAMKII promoter (AAV5.CaMKII.hChR2(H134R).eYFP, virus made by Addgene with a titer of 2.3×10^{13} GC/mL). Prior to injection, a small ~0.5 mm craniotomy was made over the area of A1 (stereotactic coordinates: 2.30 mm posterior, 4.10 mm lateral to bregma, at a depth of 0.80 mm below the pia), MGB (stereotactic coordinates: 3.05 mm posterior, 1.85 mm lateral to bregma, at a depth of 3.08 mm below the pia), or the pStr (stereotactic coordinates: 1.58 mm posterior, 3.08 mm lateral to bregma, at a depth of 3.0 mm below the pia). A glass injection pipette was tip-filled with the virus solution and lowered into the targeted brain area. 20–150 nL of the virus solution was slowly injected with a flow rate of 10 nL/s using a Drummond Nanoject III. The micropipette was left in position for 5–10 min then slowly retracted to prevent backflow of the virus along the shaft.

2–3 weeks after viral injection, mice were deeply anesthetized with isoflurane (5% for 5–8 min) and perfused transcardially with 10 mL of ice-cold cutting solution containing (in mM): 110 Choline chloride, 2.5 KCl, 25 glucose, 25 NaHCO3, 1.25 NaH2PO4, 0.5 CaCl2, 7 MgCl2, 11.6 L-ascorbic acid and 3.1 sodium pyruvate. The brain was rapidly extracted and acute 300 μm coronal slices were cut in this solution with a vibratome (Leica VT1200S) then transferred to artificial cerebrospinal fluid (ACSF) containing the following (in mM): 125 NaCl, 2.5 KCl, 25 glucose, 25 NaHCO3, 1.25 NaH2PO4, 2 CaCl2, and 1 MgCl2, Slices were incubated in ACSF at 32°C for 20 min and then stored for at least 1 h at room temperature. All solutions were constantly bubbled with 95% O2/5% CO2. For corticostriatal and thalamostriatal optogenetics, the cortex or thalamus was also sectioned and inspected to ensure that the ChR2 injection was targeted to A1 or MGB. If injections missed the target nucleus, slices were not utilized for recordings.

Targeted whole-cell recordings were made from neurons in the pStr in a region that was densely innervated by A1 or MGB as visualized by expression of YFP axons. SPNs were first identified visually by differential interference contrast (DIC) imaging. The cellular identity of targeted neurons was confirmed through expression or lack of expression of transgenically-expressed reporters. In current-clamp recordings, neurons were additionally identified as SPNs due to characteristic intrinsic properties (R_{in} 61.9 MΩ–247.2 MΩ, high rheobase values (75 pA–225 pA) and lack of spontaneous AP firing). D1 and D2 SPNs were sequentially patched, and cells were located at the same depth in the slice, less than 80 μm of each other (Figure S2D), and the recording order alternated between pairs.[46] Current-clamp and voltage-clamp recordings were performed using borosilicate pipettes (3–5 MΩ) filled with potassium- or cesium-based intracellular solution containing the following (in mM): 135 K- or Cs-methyl sulfonate, 5 KCl, 0.1 EGTA-KOH, 10 HEPES, 2 NaCl, 5 MgATP, 0.4 Na2GTP, 10 Na2-phosphocreatine and 2–4 mg/mL of biocytin. Voltage or V_m signals were amplified using a Multiclamp 700B amplifier (Axon Instruments), digitized at 20 kHz by a Digidata 1550B AD/DA board (Molecular Devices) and acquired with the pClamp 10 software (Molecular Devices).

ChR2-expressing A1 and MGB axons were stimulated optically with 8 ms-long 470 nm light from a blue light-emitting diode (CoolLED pE-4000) through a 40 × 0.8 NA objective with a power range of 0.014–1.5 mW/mm^2. For voltage-clamp experiments, responsive cells were defined by the presence of an EPSC at −80 mV in voltage-clamp configuration. Non-responsive cells were defined as not displaying a light-elicited current at the maximum of the LED power. Pairs were only recorded when both cells were connected, and the same light was used for each pair. For characterization of light-evoked EPSCs and IPSCs, 6–10 trials were averaged.

For current-clamp experiments, cells were held at their resting membrane potential, responsive cells were defined as having a PSP in response to light stimuli and the same light intensity was used for each pair. AP probability was tested in each recorded cell with lights steps ranging from 0 to 100% power, and a cell was included as having APs if it fired at any light intensity. Membrane resistances were determined by measuring the response to a voltage step command from −65 to −75 mV. Spike frequency-depolarization curves were generated by injecting a series of 500 ms depolarizing current steps increasing by 25 pA

For experiments mapping FSI (PV+) connectivity, SPNs were targeted for sequential patching as described above. Light-evoked IPSCs from PV interneurons expressing ChR2 were elicited using 2 ms-long 470 nm light pulses through a 40 × 0.8 NA objective with a power range of 0.014–0.1 mW/mm^2 and the same power level was used for each pair. For Paired-Pulse Ratio (PPR) experiments, 10 Hz light trains at minimum light stimulation was used to elicit trains of stimuli.

To determine monosynaptic input, 1 μM tetrodotoxin (TTX, HelloBio) to prevent sodic AP generation and 100 μM 4-aminopyridine (4-AP, HelloBio) to block K+ voltage-dependent channels were added to ACSF. To determine the specificity of GABAergic currents at +10 mV, 10 μM of SR95531 (HelloBio) was added to the bath.

For experiments with DREADDs in slice, D1-tdTomato x PV-Cre mice were injected with AAV-hSyn-DIO-hM4D(Gi)-mCherry (virus made by Addgene with a titer of 2.3×10^{13} GC/mL) and AAV-DIO-GFP (virus made by the UNC Vector Core with a titer of 4.4310^{12} vg/mL) in the pStr. These mice were also injected with AAV-Chronos (virus made by the Neurophotonics Platform at Université Laval with a titer of 1.2×10^{13} GC/mL) in either A1 or the MGB to allow for subsequent optogenetic circuit mapping as described above. D1 SPNs were identified based on their expression of tdTomato, PV interneurons were identified based on co-expression of mCherry and GFP and D2 SPNs were unlabeled. CNO (10 μm) was infused onto the slice and circuit mapping in current-clamp mode was carried out in D1 and D2 SPNs as described above.

Fiber photometry: PV-Cre mice were injected in the pStr with 300 nL of AAV virus expressing double-floxed inverted reading frame GCaMP8m (pGP.AAV1.syn.FLEX.jGCaMP8m.WPRE, virus made by Addgene with a titer of 2.4×10^{13} GC/mL) following the same procedure as described above. A commercially available optic fiber (400 μm diameter; numerical aperture (NA) = 0.5; RWD Life Science Co.) was implanted above the injection site and cemented to the skull with a head bar. To record the GCaMP8m signal, excitation light was passed through a fiber-optic patch cord (Doric, 400 μm, 0.48 NA) coupled to LEDs at 470 nm (Thorlabs, M470F3) connected to a fluorescence mini-cube (Doric, FMC5_E1(460–490)_F1(500–540)_E2(555–570)_F2(580–680)_S). Excitation light delivered in continuous wave mode with light power measured at the tip of the fiber-optic patch cord was set to 20–40 μW. Emission light was collected through the same patch cord and fluorescence mini-cube connected to a photoreceiver (Newport, 2151; set to DC mode). Photometry signals were digitized at 20 kHz by a National Instruments acquisition board. 3 weeks after the injection, mice underwent habituation to head fixation as described above. On the day of recording, mice were placed on the rig and photometry signals were recorded in response to each chord. Between 15 and 22 trials were collected for each chord.

For DREADDi experiments *in vivo* in which we monitored auditory-evoked responses in D2 SPNs, we crossed PV-Cre with A2A-Flp mice. These mice were injected with AAV-hSyn-DIO-hM4D(Gi)-mCherry (same as above) and AAV-EF1a-fDIO-GCaMP6f (virus made by the UNC Vector Core with a titer of 4.1×10^{12} vg/mL) and implanted with head bars. After 3 weeks to allow sufficient expression of the viruses, mice were head-fixed and exposed to white noise stimuli (100 ms bursts) at varying intensities (40 db, 60 dB, 75 dB and 90 dB). Mice were injected with either saline or CNO on subsequent days with the order of which was injected first randomized between mice. Auditory-evoked z-scored deltaF/F responses were then measured and compared between saline and CNO sessions.

Retrograde tracing: For rabies-based transsynaptic tracing from striatal neurons, 60 nL of a 1:1 mixture of AAV-FLEX-N2cG-mKate (virus made by UNC NeuroTools BRAIN Initiative Vector Core with a titer of 9.83×10^{13} GC/mL) and AAV-EF1a-FLEX-TVA-mCherry (virus made by Stanford Gene Vector and Virus Core with a titer of 9.3×10^{12} vg/mL) were injected into the pStr at a depth of 2.95–3.05 mm, 1.60–1.68 mm posterior and 3.12 mm lateral to bregma. Two weeks later, mice were injected in the same location

with 350 nL of pseudotyped, G-deficient rabies virus (virus made by Thomas Jefferson University with a titer of 2.0×10^9 ffu/mL).

Histology: Mice were deeply anesthetized with isoflurane (5% for 5–8 min, inhaled) and perfused transcardially with 4% paraformaldehyde (PFA) in 0.1 M phosphate buffered saline (PBS). Brains were removed and fixed in 4% PFA for a maximum of 24 h in the same solution, which was then replaced by a 0.1 M PBS solution. 50 μm thick coronal slices were for used for rabies experiments and PV staining, and 100 μm coronal slices were cut for *in vivo* recorded brains (vibratome, Leica VT1000S). To identify PV interneurons, slices were stained with anti-Parvalbumin antibody (1:1000, Millipore) overnight at 4°C, and incubated with a secondary antibody coupled with Alexa 647 (1:1000, ThermoFisher). To amplify the rabies injection site, slices were stained for dsRed (rabbit anti-dsRed, 1:16000, Zuckerman Institute Antibody Core, Columbia University) and incubated with a secondary antibody coupled with Alexa 594 (1:1000, Invitrogen). The slices were subsequently mounted with DAPI mounting media (Southern Biotech). Images were obtained with a custom-built Nikon AZ100 multizoom microscope, equipped with a 4× 0.4NA objective with an automated slide loader at the Columbia University Zuckerman Institute's Cellular Imaging platform.

For *in vivo* experiments, slices were cut at 100 μm and incubated with Streptavidin coupled to Alexa 647 (1:2000, Invitrogen). Images were obtained with a slide scanner (Olympus VS2000) with a 20x objective to identify the location of recorded cells.

QUANTIFICATION AND STATISTICAL ANALYSIS

***In vivo* recordings:** All data analysis of *in vivo* recordings data was performed in MATLAB using custom-written algorithms. Rheobase was reported as the minimum current injection required to elicit an AP in each cell, as determined from a protocol in which increasing current steps were elicited in steps of 50 pA to each cell. Input resistance (R_{in}) was measured as the slope of a linear fit between injected hyper-polarizing current steps (from −200 pA to 0 pA in steps of 50 pA).

To assess the auditory stimulus-triggered response, V_m changes to the same chord were evaluated relative to a baseline V_m averaged 200 ms before the stimulus and averaged. In awake experiments, a neuron was considered responsive if the baseline-subtracted Vm in the period 20–40 ms after the onset of chord presentation was at least 2 mV, had a Z score greater than or equal to 3 and the cumulative integration of the chord presentation window was greater than 3500 mV-seconds. In anesthetized experiments, the same criteria for responsiveness applied, however here we used a response window of 30–80 ms after the onset of chord presentation to account for variations in the internal temperature of the animal.

***Ex vivo* recordings:** Data analysis was performed in IgorPro (Wavemetrics) with custom-written code. Mean traces were calculated by averaging over 6 to 10 single trials. Voltage traces and membrane potential traces were aligned to the onset of the ChR2 stimulus of the MGB or A1 axons, or PV + interneurons. Mean PSC or PSP amplitudes were calculated by taking the average peak and subtracting the pre-stimulus voltage or potential. The E/I ratio was calculated for each cell individually by dividing the average EPSC by the average IPSC.

Baselines were defined as 300 ms before the stimulus onset. PPR was calculated as the ratio of the peak amplitude of the averaged current response evoked by the second, third, and fourth stimulation to the peak amplitude of the averaged current response evoked by the first stimulation.

Automated anatomical reconstruction: Image processing and analysis was performed using BrainJ, a collection of custom tools developed to facilitate automated whole-brain analysis of tissue sections, as previously described.[49] Briefly, tissue sections were first arranged anterior-posterior and processed to remove external fluorescence and neighboring objects. Subsequently, sections are centered and oriented to facilitate 2D rigid body registration[50] to make a 3-D brain volume. Starter cells were identified as those that co-express dsRed (or mKate/mCherry) and GFP and were hand-counted in each slice containing cells expressing the helper and rabies viruses using the ImageJ software. Cell bodies of projecting neurons (expressing GFP) were detected using Ilastik[51], a machine learning-based pixel classification approach on images that had background fluorescence subtracted using a rolling ball filter. Data was output from the BrainJ pipeline the form of CSV files containing measurements of cell body counts from each region in the Allen Brain Atlas Common Coordinate Framework. These measurements were organized so that analyses from all brain sub-regions could be performed in the Allen Institute Mouse Common Coordinate Framework. Custom-written code in MATLAB was then used to calculate the relative ratio of cells in each brain region and compare between D1-Cre and A2A-Cre rabies-injected animals.

Fiber photometry: Raw photometry signals were processed using an available MATLAB code. In brief, raw voltage signals were down-sampled to 50 Hz (above the Nyquist frequency to prevent aliasing), and the final photometry signal (output as a percentage) was obtained using the equation $\Delta F/F = (F - F0)/F0$, in which F0 is baseline fluorescence as described (Krok et al. 2023). The latter was computed by interpolating the bottom percentile of fluorescence values measured in 30-second-long sliding windows (0% overlap) along the entire photometry trace. Sensory responses to auditory stimuli in PV interneurons were first sorted according to chord number and then averaged for all trials across the 3 mice within chords to calculate response amplitude.

Statistical analysis: Data are presented as mean ± SEM. Statistical analyses were performed using Prism 9 (GraphPad) and MATLAB custom code. The normality of data distribution was tested using the D'Agostino & Pearson test. For unpaired datasets, two-tailed Student's T-tests (for normally distributed datasets) or Mann–Whitney tests (for nonnormally distributed datasets) were employed. For paired datasets, two-tailed Student's Paired *T* test or Wilcoxon Signed-Rank test (for nonnormally distributed datasets) were employed. For multiple comparisons, we used two-Way ANOVA followed by Sidak's test. Values of $p < 0.05$ were considered statistically significant. *p* values are reported as follows: $*p < 0.05$; $**p < 0.01$; $***p < 0.001$; $****p < 0.0001$. In all plots, unless otherwise noted, errors are plotted as ±SEM.

Supplementary Material

Refer to Web version on PubMed Central for supplementary material.

ACKNOWLEDGMENTS

This work was supported by the National Institutes of Health (R01 NS126391), the Brain and Behavior Research Foundation Career Award for Medical Scientists (BBRF CAMS 1018390), and the Whitehall Foundation (research project grant #2021-12-091) to T.S.; the Leon Levy Foundation Fellowship to M.D.; and the NYU Clinical and Translational Research TL1 to M.K. CVS-N2c rabies viruses were produced by the Center for Neuroanatomy with Neurotropic Viruses, supported by P40 OD010996. We thank Nicolas Tritsch and Richard Tsien for comments on the manuscript; Anders Nelson and Akira Fushiki for technical help with rabies tracing; Susan Brenner-Morton from the Columbia Zuckerman Antibody Core; Darcy Peterka, Luke Hammond, and the Columbia Zuckerman Imaging Core for help with anatomical tracing analysis; Vincent Robert for Igor Pro code; and Rui Costa for guidance on this project.

REFERENCES

1. Wilson CJ (1987). Morphology and synaptic connections of crossed corticostriatal neurons in the rat. J. Comp. Neurol 263, 567–580. 10.1002/cne.902630408. [PubMed: 2822779]
2. Hunnicutt BJ, Jongbloets BC, Birdsong WT, Gertz KJ, Zhong H, and Mao T (2016). A comprehensive excitatory input map of the striatum reveals novel functional organization. Elife 5, e19103. 10.7554/eLife.19103. [PubMed: 27892854]
3. Hintiryan H, Foster NN, Bowman I, Bay M, Song MY, Gou L, Yamashita S, Bienkowski MS, Zingg B, Zhu M, et al. (2016). The mouse cortico-striatal projectome. Nat. Neurosci 19, 1100–1114. 10.1038/nn.4332https://www.nature.com/articles/nn.4332#supplementary-information. [PubMed: 27322419]
4. Johansson Y, and Silberberg G (2020). The Functional Organization of Cortical and Thalamic Inputs onto Five Types of Striatal Neurons Is Determined by Source and Target Cell Identities. Cell Rep. 30, 1178–1194.e3. 10.1016/j.celrep.2019.12.095. [PubMed: 31995757]
5. Albin RL, Young AB, and Penney JB (1989). The functional anatomy of basal ganglia disorders. Trends Neurosci. 12, 366–375. 10.1016/0166-2236(89)90074-X. [PubMed: 2479133]
6. Cui G, Jun SB, Jin X, Pham MD, Vogel SS, Lovinger DM, and Costa RM (2013). Concurrent activation of striatal direct and indirect pathways during action initiation. Nature 494, 238–242. 10.1038/nature11846. [PubMed: 23354054]
7. Isomura Y, Takekawa T, Harukuni R, Handa T, Aizawa H, Takada M, and Fukai T (2013). Reward-modulated motor information in identified striatum neurons. J. Neurosci 33, 10209–10220. 10.1523/JNEUROSCI.0381-13.2013. [PubMed: 23785137]
8. Parker JG, Marshall JD, Ahanonu B, Wu Y-W, Kim TH, Grewe BF, Zhang Y, Li JZ, Ding JB, Ehlers MD, and Schnitzer MJ (2018). Diametric neural ensemble dynamics in parkinsonian and dyskinetic states. Nature 557, 177–182. 10.1038/s41586-018-0090-6. [PubMed: 29720658]
9. Maltese M, March JR, Bashaw AG, and Tritsch NX (2021). Dopamine differentially modulates the size of projection neuron ensembles in the intact and dopamine-depleted striatum. Elife 10, e68041. 10.7554/eLife.68041. [PubMed: 33983121]
10. Sippy T, Lapray D, Crochet S, and Petersen CCH (2015). Cell-Type-Specific Sensorimotor Processing in Striatal Projection Neurons during Goal-Directed Behavior. Neuron 88, 298–305. 10.1016/j.neuron.2015.08.039. [PubMed: 26439527]
11. Petersen CCH (2017). Whole-Cell Recording of Neuronal Membrane Potential during Behavior. Neuron 95, 1266–1281. 10.1016/j.neuron.2017.06.049. [PubMed: 28910617]
12. Gong S, Doughty M, Harbaugh CR, Cummins A, Hatten ME, Heintz N, and Gerfen CR (2007). Targeting Cre Recombinase to Specific Neuron Populations with Bacterial Artificial Chromosome Constructs. J. Neurosci 27, 9817–9823. 10.1523/JNEUROSCI.2707-07.2007. [PubMed: 17855595]

13. Madisen L, Mao T, Koch H, Zhuo J.m., Berenyi A, Fujisawa S, Hsu Y-WA, Garcia AJ, Gu X, Zanella S, et al. (2012). A toolbox of Cre-dependent optogenetic transgenic mice for light-induced activation and silencing. Nat. Neurosci 15, 793–802. 10.1038/nn.3078. [PubMed: 22446880]
14. Ketzef M, Spigolon G, Johansson Y, Bonito-Oliva A, Fisone G, and Silberberg G (2017). Dopamine Depletion Impairs Bilateral Sensory Processing in the Striatum in a Pathway-Dependent Manner. Neuron 94, 855–865.e5. 10.1016/j.neuron.2017.05.004. [PubMed: 28521136]
15. Alegre-Cortés J, Sáez M, Montanari R, and Reig R (2021). Medium spiny neurons activity reveals the discrete segregation of mouse dorsal striatum. Elife 10, e60580. 10.7554/eLife.60580. [PubMed: 33599609]
16. de la Torre-Martinez R, Ketzef M, and Silberberg G (2023). Ongoing movement controls sensory integration in the dorsolateral striatum. Nat. Commun 14, 1004. 10.1038/s41467-023-36648-0. [PubMed: 36813791]
17. Sippy T, Chaimowitz C, Crochet S, and Petersen CCH (2021). Cell type-specific membrane potential changes in dorsolateral striatum accompanying reward-based sensorimotor learning. Function 2, zqab049. 10.1093/function/zqab049. [PubMed: 35330797]
18. Stern EA, Jaeger D, and Wilson CJ (1998). Membrane potential synchrony of simultaneously recorded striatal spiny neurons in vivo. Nature 394, 475–478. 10.1038/28848. [PubMed: 9697769]
19. Mahon S, Deniau JM, and Charpier S (2001). Relationship between EEG potentials and intracellular activity of striatal and cortico-striatal neurons: an in vivo study under different anesthetics. Cereb. Cortex 11, 360–373. 10.1093/cercor/11.4.360. [PubMed: 11278199]
20. Reig R, and Silberberg G (2014). Multisensory Integration in the Mouse Striatum. Neuron 83, 1200–1212. 10.1016/j.neuron.2014.07.033. [PubMed: 25155959]
21. Gerfen CR, and Surmeier DJ (2011). Modulation of striatal projection systems by dopamine. Annu. Rev. Neurosci 34, 441–466. 10.1146/annurev-neuro-061010-113641. [PubMed: 21469956]
22. Wickersham IR, Lyon DC, Barnard RJO, Mori T, Finke S, Conzelmann K-K, Young JAT, and Callaway EM (2007). Monosynaptic restriction of transsynaptic tracing from single, genetically targeted neurons. Neuron 53, 639–647. 10.1016/j.neuron.2007.01.033. [PubMed: 17329205]
23. Reardon TR, Murray AJ, Turi GF, Wirblich C, Croce KR, Schnell MJ, Jessell TM, and Losonczy A (2016). Rabies Virus CVS-N2c(DG) Strain Enhances Retrograde Synaptic Transfer and Neuronal Viability. Neuron 89, 711–724. 10.1016/j.neuron.2016.01.004. [PubMed: 26804990]
24. Mallet N, Le Moine C, Charpier S, and Gonon F (2005). Feedforward Inhibition of Projection Neurons by Fast-Spiking GABA Interneurons in the Rat Striatum In Vivo. J. Neurosci 25, 3857–3869. 10.1523/JNEUROSCI.5027-04.2005. [PubMed: 15829638]
25. Berke JD (2011). Functional Properties of Striatal Fast-Spiking Interneurons. Front. Syst. Neurosci 5, 45. [PubMed: 21743805]
26. Bennett BD, and Bolam JP (1994). Synaptic input and output of parvalbumin-immunoreactive neurons in the neostriatum of the rat. Neuroscience 62, 707–719. 10.1016/0306-4522(94)90471-5. [PubMed: 7870301]
27. Hippenmeyer S, Vrieseling E, Sigrist M, Portmann T, Laengle C, Ladle DR, and Arber S (2005). A developmental switch in the response of DRG neurons to ETS transcription factor signaling. PLoS Biol. 3, e159. 10.1371/journal.pbio.0030159. [PubMed: 15836427]
28. Filipović M, Ketzef M, Reig R, Aertsen A, Silberberg G, and Kumar A (2019). Direct pathway neurons in mouse dorsolateral striatum in vivo receive stronger synaptic input than indirect pathway neurons. J. Neurophysiol 122, 2294–2303. 10.1152/jn.00481.2019. [PubMed: 31618095]
29. Sheng MJ, Lu D, Shen ZM, and Poo MM (2019). Emergence of stable striatal D1R and D2R neuronal ensembles with distinct firing sequence during motor learning. Proc. Natl. Acad. Sci. USA 116, 11038–11047. 10.1073/pnas.1901712116. [PubMed: 31072930]
30. Chen APF, Chen L, Shi KW, Cheng E, Ge S, and Xiong Q (2023). Nigrostriatal dopamine modulates the striatal-amygdala pathway in auditory fear conditioning. Nat. Commun 14, 7231. 10.1038/s41467-023-43066-9. [PubMed: 37945595]
31. Kintscher M, Kochubey O, and Schneggenburger R (2023). A striatal circuit balances learned fear in the presence and absence of sensory cues. Elife 12, e75703. 10.7554/eLife.75703. [PubMed: 36655978]

32. Gritton HJ, Howe WM, Romano MF, DiFeliceantonio AG, Kramer MA, Saligrama V, Bucklin ME, Zemel D, and Han X (2019). Unique contributions of parvalbumin and cholinergic interneurons in organizing striatal networks during movement. Nat. Neurosci 22, 586–597. 10.1038/s41593-019-0341-3. [PubMed: 30804530]
33. O'Hare JK, Li H, Kim N, Gaidis E, Ade K, Beck J, Yin H, and Calakos N (2017). Striatal fast-spiking interneurons selectively modulate circuit output and are required for habitual behavior. Elife 6, e26231. 10.7554/eLife.26231. [PubMed: 28871960]
34. Owen SF, Berke JD, and Kreitzer AC (2018). Fast-Spiking Interneurons Supply Feedforward Control of Bursting, Calcium, and Plasticity for Efficient Learning. Cell 172, 683–695.e15. 10.1016/j.cell.2018.01.005. [PubMed: 29425490]
35. Kawaguchi Y, Wilson CJ, Augood SJ, and Emson PC (1995). Striatal interneurones: chemical, physiological and morphological characterization. Trends Neurosci. 18, 527–535. 10.1016/0166-2236(95)98374-8. [PubMed: 8638293]
36. Koós T, and Tepper JM (1999). Inhibitory control of neostriatal projection neurons by GABAergic interneurons. Nat. Neurosci 2, 467–472. 10.1038/8138. [PubMed: 10321252]
37. Ramanathan S, Hanley JJ, Deniau J-M, and Bolam JP (2002). Synaptic convergence of motor and somatosensory cortical afferents onto GABAergic interneurons in the rat striatum. J. Neurosci 22, 8158–8169. 10.1523/JNEUROSCI.22-18-08158.2002. [PubMed: 12223570]
38. Tepper JM, Wilson CJ, and Koós T (2008). Feedforward and feedback inhibition in neostriatal GABAergic spiny neurons. Brain Res. Rev 58, 272–281. 10.1016/j.brainresrev.2007.10.008. [PubMed: 18054796]
39. Silberberg G, and Bolam JP (2015). Local and afferent synaptic pathways in the striatal microcircuitry. Curr. Opin. Neurobiol 33, 182–187. 10.1016/j.conb.2015.05.002. [PubMed: 26051382]
40. Fino E, Vandecasteele M, Perez S, Saudou F, and Venance L (2018). Region-specific and state-dependent action of striatal GABAergic interneurons. Nat. Commun 9, 3339. 10.1038/s41467-018-05847-5. [PubMed: 30131490]
41. Menegas W, Babayan BM, Uchida N, and Watabe-Uchida M (2017). Opposite initialization to novel cues in dopamine signaling in ventral and posterior striatum in mice. Elife 6, e21886. 10.7554/eLife.21886. [PubMed: 28054919]
42. Chen APF, Malgady JM, Chen L, Shi KW, Cheng E, Plotkin JL, Ge S, and Xiong Q (2022). Nigrostriatal dopamine pathway regulates auditory discrimination behavior. Nat. Commun 13, 5942. 10.1038/s41467-022-33747-2. [PubMed: 36209150]
43. Menegas W, Akiti K, Amo R, Uchida N, and Watabe-Uchida M (2018). Dopamine neurons projecting to the posterior striatum reinforce avoidance of threatening stimuli. Nat. Neurosci 21, 1421–1430. 10.1038/s41593-018-0222-1. [PubMed: 30177795]
44. Zhou FM, Liang Y, and Dani JA (2001). Endogenous nicotinic cholinergic activity regulates dopamine release in the striatum. Nat. Neurosci 4, 1224–1229. 10.1038/nn769. [PubMed: 11713470]
45. Liu C, Cai X, Ritzau-Jost A, Kramer PF, Li Y, Khaliq ZM, Hallermann S, and Kaeser PS (2022). An action potential initiation mechanism in distal axons for the control of dopamine release. Science 375, 1378–1385. 10.1126/science.abn0532. [PubMed: 35324301]
46. Krok AC, Maltese M, Mistry P, Miao X, Li Y, and Tritsch NX (2023). Intrinsic dopamine and acetylcholine dynamics in the striatum of mice. Nature 621, 543–549. 10.1038/s41586-023-05995-9. [PubMed: 37558873]
47. Gittis AH, Hang GB, LaDow ES, Shoenfeld LR, Atallah BV, Fink-beiner S, and Kreitzer AC (2011). Rapid Target-Specific Remodeling of Fast-Spiking Inhibitory Circuits after Loss of Dopamine. Neuron 71, 858–868. 10.1016/j.neuron.2011.06.035. [PubMed: 21903079]
48. Alexander GE, and Crutcher MD (1990). Functional architecture of basal ganglia circuits: neural substrates of parallel processing. Trends Neurosci. 13, 266–271. [PubMed: 1695401]
49. Botta P, Fushiki A, Vicente AM, Hammond LA, Mosberger AC, Gerfen CR, Peterka D, and Costa RM (2020). An Amygdala Circuit Mediates Experience-Dependent Momentary Arrests during Exploration. Cell 183, 605–619.e22. 10.1016/j.cell.2020.09.023. [PubMed: 33031743]

50. Thévenaz P, Ruttimann UE, and Unser M (1998). A pyramid approach to subpixel registration based on intensity. IEEE Transactions on Image Processing 7, 27–41. 10.1109/83.650848. [PubMed: 18267377]

51. Sommer C, Straehle C, Köthe U, and Hamprecht FA (2011). Ilastik: Interactive learning and segmentation toolkit. In 2011 IEEE International Symposium on Biomedical Imaging: From Nano to Macro, pp. 230–233. 10.1109/ISBI.2011.5872394.

Highlights

- We compare auditory-evoked responses in posterior striatum direct and indirect pathways
- Direct pathway neurons show larger auditory-evoked responses *in vivo* and *ex vivo*
- Synapses from primary auditory areas show a larger E/I ratio onto direct pathway neurons
- Differences in PV+ interneuron connectivity onto these pathways underlie these effects

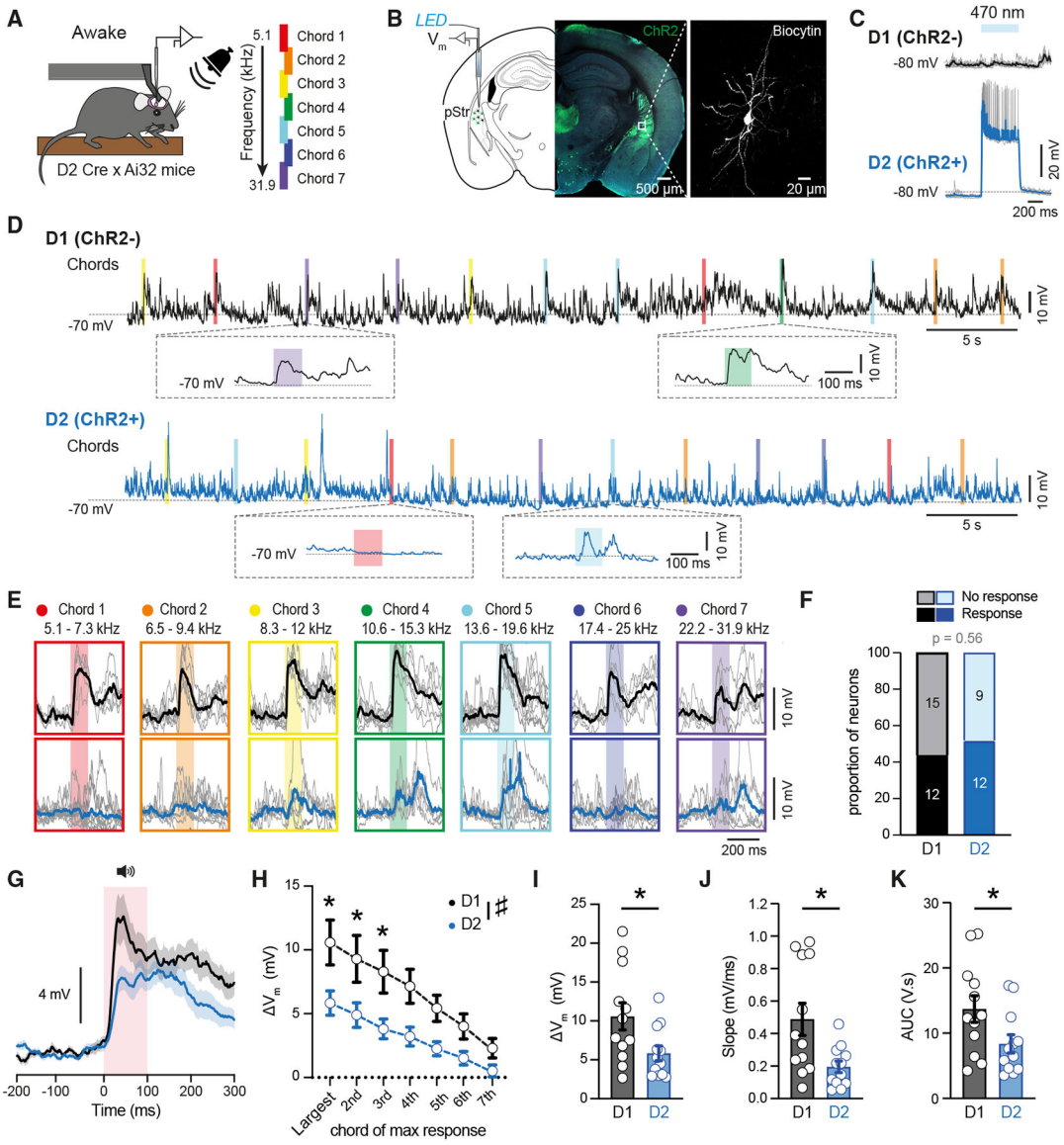

Figure 1. Cell-type-specific auditory-evoked responses in the pStr in awake mice

(A) Mice were head fixed for V_m recordings during sound presentation.

(B) Neurons were targeted for recordings in the pStr of D2-ChR2-YFP-mice (left), which enabled optogenetic identification. Biocytin allowed for post hoc identification and its precise location (right).

(C) Top: a ChR2−, putative D1 SPN (black) that did not respond with depolarization. Bottom: a ChR2+ D2 SPN that responded with depolarization and AP firing (blue).

(D) Example V_m trace from a D1 SPN (top, black) and D2 SPN (bottom, blue). Vertical colored bars indicate chord presentations.

(E) V_m of the D1 SPN (top row, black) and D2 SPN (bottom row, blue) shown in (D) for all trials in response to all chords (black and blue average, gray individual trials).

(F) Proportion of D1 and D2 SPNs responsive to at least one chord. Statistical significance between D1 and D2 SPNs was assessed using a chi-square test.

(G) Grand average V_m of all responsive D1 (black, $n = 12$) and D2 SPNs (blue, $n = 12$) of the chord that yielded the maximum response in each neuron.
(H) Average V_m response of D1 SPNs (black) and D2 SPNs (blue) to the chord that yielded the maximum response and the subsequent chords that yielded progressively smaller responses. Statistical significance between D1 and D2 SPNs was calculated using a two-way ANOVA with Sidhak's *post hoc* test for each chord (#$p < 0.05$, *$p < 0.05$). Each open circle represents the average data from all D1 SPNs (black, $n = 12$) and D2 SPNs (blue, $n = 12$).
(I) The maximum delta V_m was larger in D1 SPNs as assessed by a Student's *t* test (*$p < 0.05$; $n = 12$). Each open circle represents an individual cell (black, D1 SPNs, $n = 12$; blue, D2 SPNs, $n = 12$).
(J) The slope of the response was significantly larger in D1 SPNs as assessed by a Student's *t* test (*$p < 0.05$). Each open circle represents an individual cell (black, D1 SPNs, $n = 12$; blue, D2 SPNs, $n = 12$).
(K) The area under the curve (AUC) during the first 50 ms was larger in D1 SPNs as assessed by a Student's *t* test (*$p < 0.05$). Each open circle represents an individual cell (black, D1 SPNs, $n = 12$; blue, D2 SPNs, $n = 12$).
All data are represented as mean ± SEM.

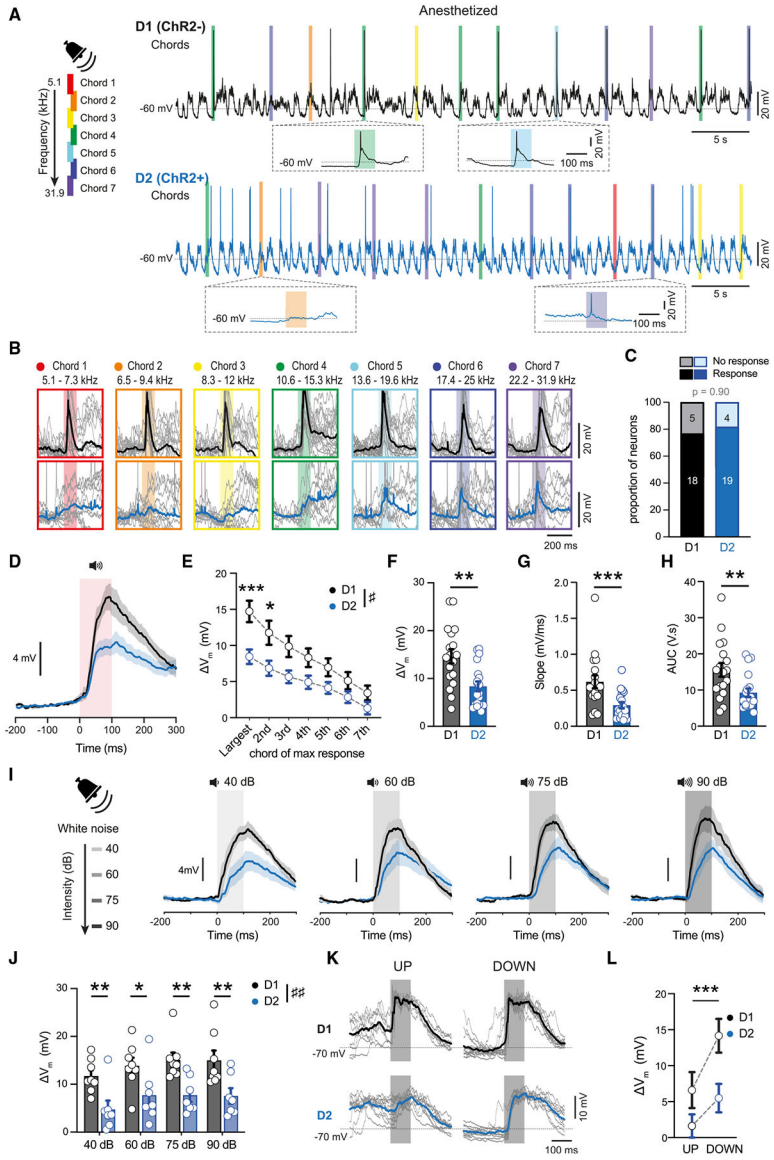

Figure 2. Cell-type-specific auditory-evoked responses in the pStr in anesthetized mice

(A) Example of V_m recordings in a D1 SPN (top, black) and D2 SPN (bottom, blue) in anesthetized mice; vertical colored bars represent chord presentations.

(B) V_m of the D1 SPN (top) and D2 SPN (bottom) shown in (A) for all trials in response to all chords (black and blue average, gray individual trials).

(C) Proportion of D1 and D2 SPNs responsive to at least one chord. Statistical significance between D1 and D2 SPNs was assessed using a chi-square test.

(D) Grand average V_m of all responsive D1 (black, $n = 18$) and D2 (blue, $n = 19$) SPNs of the chord that yielded the maximum response in each neuron.

(E) Average V_m response of D1 SPNs (black) and D2 SPNs (blue) to the chord that yielded the maximum response and the subsequent chords that yielded progressively smaller responses. Statistical significance between D1 and D2 SPNs was calculated using a two-way ANOVA with Sidhak's *post hoc* test for each chord (#$p < 0.05$, *$p < 0.05$, ***$p < 0.001$).

Each open circle represents the average data from all D1 SPNs (black, $n = 18$) and D2 SPNs (blue, $n = 19$).

(F) The maximum delta V_m was larger in D1 SPNs in anesthetized mice as assessed by a Student's *t* test (**$p < 0.01$). Each open circle represents an individual cell (black, D1 SPNs, $n = 18$; blue, D2 SPNs, $n = 19$).

(G) The slope of the response was larger in D1 SPNs as assessed by a Mann Whitney U test (***$p < 0.001$). Each open circle represents an individual cell (black, D1 SPNs, $n = 18$; blue, D2 SPNs, $n = 19$).

(H) The AUC of the stimulus-triggered response was significantly larger in D1 SPNs as assessed by a Student's *t* test (**$p < 0.01$). Each open circle represents an individual cell (black, D1 SPNs, $n = 18$; blue, D2 SPNs, $n = 19$).

(I) Left: white noise bursts were played to anesthetized mice. Right: grand average V_m responses of D1 SPNs (black, $n = 8$) and D2 SPNs (blue, $n = 7$).

(J) D1 SPNs responded to white noise bursts with a significantly higher amplitude than D2 SPNs. Statistical significance between D1 and D2 SPNs was calculated using a two-way ANOVA with Sidhak's *post hoc* test for each intensity (##$p < 0.01$, *$p < 0.05$, **$p < 0.01$). Each open circle represents the average data from all D1 SPNs (black, $n = 8$) and D2 SPNs (blue, $n = 7$).

(K) Example evoked V_m responses from a D1 SPN (top, black) and D2 SPN (bottom, blue) triggered during UP states and DOWN states.

(L) Responses of D1 and D2 SPNs were larger in the DOWN state than in the UP state. Statistical significance between UP and DOWN state was calculated using a two-way ANOVA (***$p < 0.001$). Each open circle represents the average data from all D1 SPNs (black, $n = 8$) and D2 SPNs (blue, $n = 7$).

All data are represented as mean ± SEM.

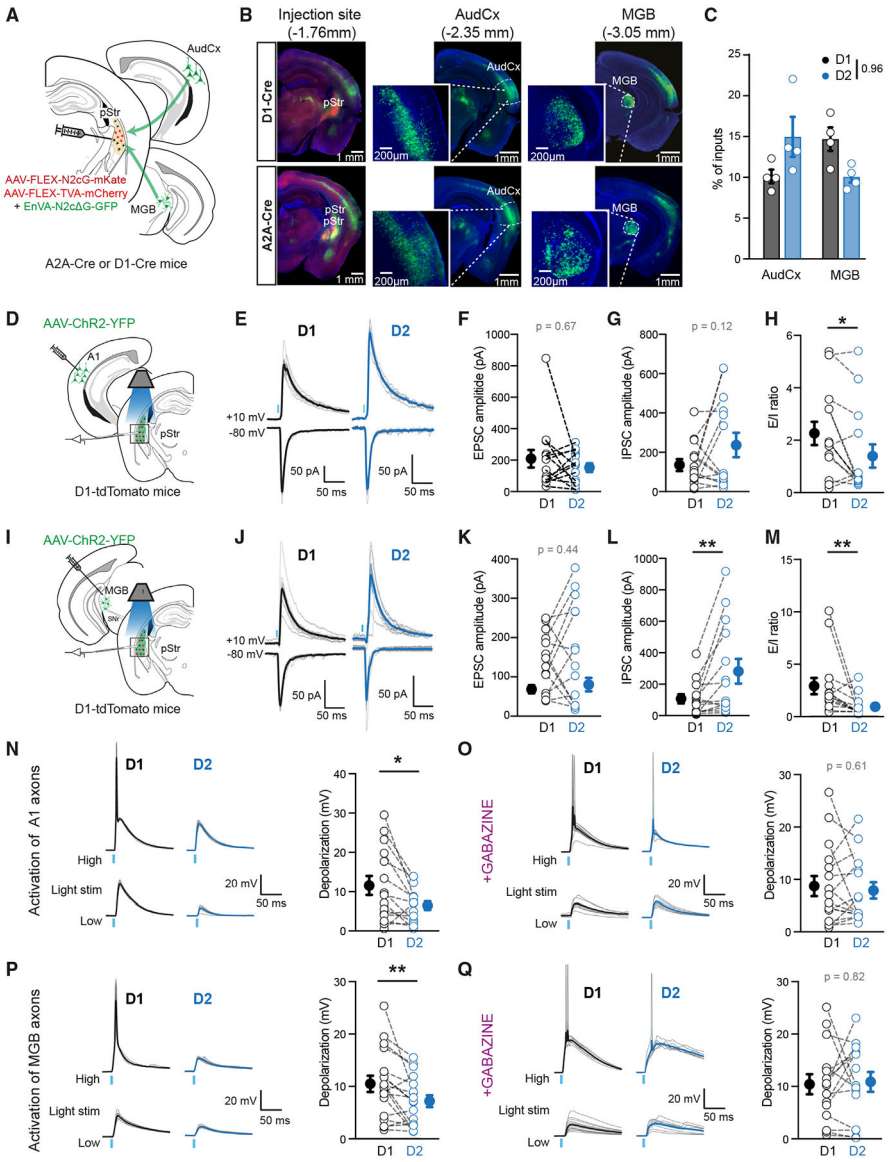

Figure 3. Cell-type-specific connectivity from the thalamus and cortex to the pStr

(A) Schematic illustrating rabies injection into the pStr of A2A-Cre or D1-Cre mice, labeling monosynaptic inputs from throughout the brain, including the auditory thalamus (MGB) and primary auditory cortex (A1).

(B) Cells infected with helper viruses in the pStr were labeled with mCherry and mKate, while neurons monosynaptically connected were labeled with GFP.

(C) The percentages of cells projecting from A1 and MGB onto D1 and D2 SPNs were similar as assessed by a two-way RM Anova.

(D) In mice where A1 was injected with ChR2, D1 and D2 SPNs were sequentially targeted for patch clamp in the region of the pStr that showed the highest density of axons.

(E) Example EPSCs elicited at −80 mV (bottom) IPSCs recorded at +10 mV in D1 SPNs (left, black) and D2 SPNs (right, blue). Gray traces are individual trials.

(F) A1 light-evoked EPSC amplitudes were not significantly different between D1 and D2 SPNs as assessed by a Wilcoxin matched pairs test. Each open circle represents an individual cells, filled circles are the average (black, D1 SPNs; blue, D2 SPNs, $n = 14$ pairs).
(G) A1 light-evoked IPSC amplitudes were not significantly different between D1 and D2 SPNs as assessed by a Student's paired t test. Each open circle represents an individual cell, filled circles are the average (black, D1; blue, D2 SPNs, $n = 14$ pairs).
(H) The A1 light-evoked E/I ratio was significantly larger in D1 SPNs as assessed by a Wilcoxin matched pairs test ($*p < 0.05$). Each open circle represents an individual cells, filled circles are the average (black, D1 SPNs; blue, D2 SPNs, $n = 14$ pairs).
(I) Same as (D) but with MGB injection.
(J) Same as (E) but with MGB axon stimulation.
(K) MGB light-evoked EPSC amplitudes were not significantly different between D1 and D2 SPNs as assessed by a Student's paired t test. Each open circle represents an individual cell, filled circles are the average (black, D1 SPNs; blue, D2 SPNs, $n = 14$ pairs).
(L) MGB light-evoked IPSC amplitude was significantly larger in D2 SPNs as assessed by a Wilcoxin matched pairs test ($**p < 0.01$). Each open circle represents an individual cells, filled circles are the average (black, D1; blue, D2 SPNs, $n = 14$ pairs).
(M) The A1 light-evoked E/I ratio was larger in D1 SPNs as assessed by a Wilcoxin matched pairs test ($**p < 0.01$). Each open circle represents an individual cells, filled circles are the average (black, D1 SPNs; blue, D2 SPNs, $n = 14$ pairs).
(N) Left: example traces of A1 light-evoked PSPs evoked with high (top) and low (bottom) light intensity in D1 (left, black) and D2 SPNs (right, blue). Individual trials are shown in gray. Right: PSP amplitude was significantly larger in D1 SPNs as assessed by a Student's paired t test ($*p < 0.01$). Each open circle represents an individual cell, filled circles are the average (black, D1 SPNs; blue, D2 SPNs, $n = 15$ pairs).
(O) Left: same as (N) but with inhibitory transmission blocked with gabazine. Right: with inhibitory transmission blocked, the A1-evoked PSP amplitude is not different between D1 and D2 SPNs as assessed by a Student's paired t test. Each open circle represents an individual cell, filled circles are the average (black, D1 SPNs; blue, D2 SPNs, $n = 16$ pairs).
(P) Same as (N) but with MGB stimulation. The difference between D1 and D2 SPNs was assessed using a Student's paired t test ($**p < .01$; black, D1 SPNs; blue, D2 SPNs, $n = 18$ pairs).
(Q) Same as (O) but with MGB stimulation. The difference between D1 and D2 SPNs was assessed using a Student's paired t test (D1 SPNs, $n = 15$; D2 SPNs, $n = 15$).
All data are represented as mean ± SEM.

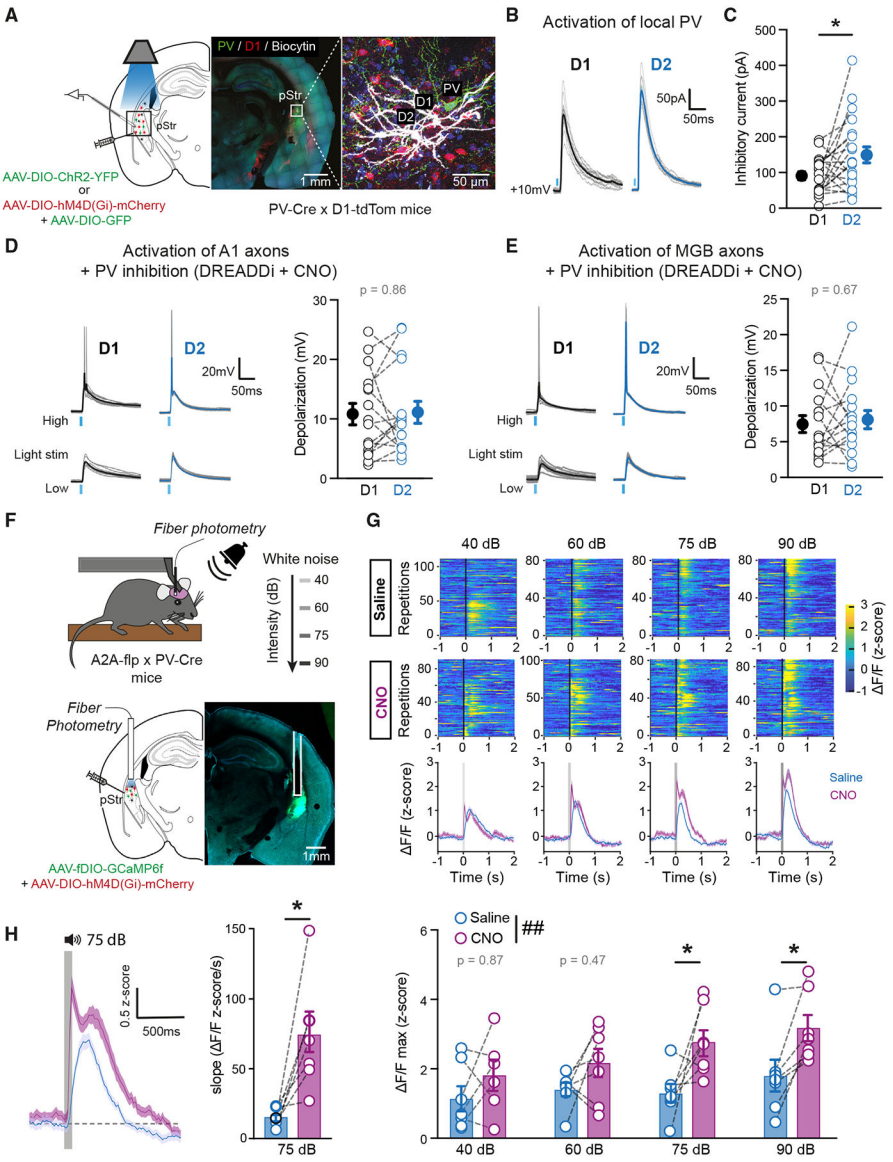

Figure 4. PV interneurons modulate the auditory-evoked responses of D1 and D2 SPNs

(A) Optogenetic circuit mapping and DREADD inhibition of PV+ interneuron connectivity onto D1 and D2 SPNs in the pStr.

(B) Example traces of PV light-evoked IPSCs in D1 (left, black) and D2 SPNs (right, blue); gray traces are individual trials.

(C) PV light-evoked IPSC amplitudes were larger in D2 SPNs than in D1 SPNs as assessed using a Student's paired *t* test (*$p < 0.05$). Each open circle represents an individual cell, filled circles are the average (black, D1 SPNs; blue, D2 SPNs, $n = 21$ pairs).

(D) Activation of A1 axons in slices where PV+ interneurons were infected with an inhibitory DREADD (hM4D(Gi)) activated by CNO resulted in similar EPSP responses in D1 and D2 SPNs as assessed by a Student's paired *t* test. Each open circle represents an individual cell, filled circles are the average (black, D1 SPNs; blue, D2 SPNs, $n = 16$ pairs)

(E) Same as (D) but for MGB stimulation. The difference between D1 and D2 SPNs was assessed using a Student's paired *t*-test. Each open circle represents an individual cell, filled circles are the average (black, D1 SPNs; blue, D2 SPNs, $n = 16$ pairs).
(F) Mice were head fixed for fiber photometry recordings. GCaMP6f was expressed in D2 SPNs and hM4D(Gi) was expressed in PV interneurons.
(G) Top: raster plost showing *z*-scored deltaF/F photomtery responses of all repititions of white noise stimuli at 4 intensities. Middle: average *z*-score deltaF/F in saline (blue) and CNO (magenta). Bottom: maximum *z*-scored deltaF/F in saline vs. CNO conditions was significantly different as assessed by a two-way ANOVA with Sidhak's *post hoc* test for each intensity ($\#\#p < 0.01$, $*p < 0.05$). Each open circle represents the data from one mouse (blue, saline; magenta, CNO, $n = 7$ pairs).
(H) Left: expanded average *Z* scored ΔF/F from (G) at 75 dB in saline (blue) and CNO (magenta). Right: the slope of this response in the first 100 ms was significantly faster with CNO as assessed by a Wilcoxin matched pairs test ($*p < 0.05$). Each open circle represents the data from one mouse (blue, saline; magenta, CNO, $n = 7$ pairs).
All data are represented as mean ± SEM.

KEY RESOURCES TABLE

REAGENT or RESOURCE	SOURCE	IDENTIFIER
Antibodies		
Streptavidin, Alexa Fluor 647 conjugate	ThermoFisher	S21374
Mouse anti-Parvalbumin	Millipore	RRID: AB_2174013
Rabbit anti-dsRed	Zuckerman Institute Antibody Core, Columbia University	RRID: AB_3086780
Donkey anti-Rabbit Alexa 594	ThermoFisher	RRID: AB_141637
Donkey anti-Mouse Alexa 647	ThermoFisher	RRID: AB_2762830
Bacterial and virus strains		
AAV5-CaMKII-hChR2(H134R)-eYFP	Addgene	26969-AAV5
AAV2-Ef1a-DIO-hChR2(H134R)-eYFP	UNC Vector Core/Deisseroth	AV4378P
AAV2-CAG-FLEX-N2cG-mKate2.0	UNC NeuroTools BRAIN Initiative Vector Core	N/A
AAV-EF1a-FLEX-TVA-mCherry	Stanford Gene Vector and Virus Core	GVVC-AAV-067
EnVA-N2cΔG-GFP	Thomas Jefferson University	N/A
pGP-AAV1-syn-FLEX-jGCaMP8m-WPRE	Addgene	162375-AAV1
AAV2/5-CaMKII-Chronos-GFP	Neurophotonics Platform, Université Laval	319-AAV5
AAV-hSyn-DIO-hM4D(Gi)-mCherry	Addgene	44362-AAV5
AAV-CAG-FLEX-eGFP	UNC Vector Core/Boyden	AV5294B
AAV-EF1a-fDIO-GCaMP6f	UNC Vector Core/Deisseroth	AV8613
Chemicals, peptides, and recombinant proteins		
Biocytin	Biotium	90055
TTX	Hello Bio	HB1035
4-AP	Hello Bio	HB1073
SR95531	Hello Bio	HB0901
CNO	Hello Bio	HB6149
Deposited data		
Data and analysis code	This study	zenodo:https://doi.org/10.5281/zenodo.10641633.
Experimental models: Organisms/strains		
D2-Cre: B6.FVB(Cg)-Tg(Drd2-cre)ER44Gsat/Mmucd	MMRRC: UCD	RRID:MMRRC_032108-UCD
A2A-Cre: B6.FVB(Cg)-Tg(Adora2a-cre)KG139Gsat/Mmucd	MMRRC: UCD	RRID:MMRRC_036158-UCD
D1-Cre (EY262): B6.FVB(Cg)-Tg(Drd1-cre)EY262Gsat/Mmucd	MMRRC: UCD	RRID:MMRRC_030989-UCD
Drd1a-tdTomato: B6.Cg-Tg(Drd1a-tdTomato)6Calak/J	The Jackson Laboratory	RRID:IMSR_JAX:016204
Ai32: *B6.Cg-Gt(ROSA)26Sor*$^{tm32(CAG-COP4*H134R/EYFP)Hze}$/J	The Jackson Laboratory	RRID:IMSR_JAX:024109
Ai14: *B6.Cg-Gt(ROSA)26Sor*$^{tm14(CAG-tdTomato)Hze}$/J	The Jackson Laboratory	RRID:IMSR_JAX:007914
Ai9: *B6.Cg-Gt(ROSA)26Sor*$^{tm9(CAG-tdTomato)Hze}$/J	The Jackson Laboratory	RRID:IMSR_JAX:007909
PV-Cre: *B6.129P2-Pvalb*$^{tm1(cre)Arbr}$/J	The Jackson Laboratory	RRID:IMSR_JAX:017320
A2A-Flp	Generated by the laboratory of R. Costa at Columbia University	N/A

REAGENT or RESOURCE	SOURCE	IDENTIFIER
Software and algorithms		
ImageJ	https://imagej.net/	RRID:SCR_003070
MATLAB	MathWorks	RRID:SCR_001622
IgorPro	Wavemetrics	RRID:SCR_000325
pClamp 11	MolecularDevices	RRID:SCR_011323
GraphPad Prism 8	http://www.graphpad.com/	RRID:SCR_002798
BrainJ	Botta et al.[49]	N/A
Other		
Custom code (MATLAB)	This paper	Zenodo
Custom code (IgorPro)	This paper	Zenodo
Optopatcher	A-M Systems	663849